

A hot terrestrial planet orbiting the bright M dwarf L 168-9 unveiled by TESS ★,★★,★★★

N. Astudillo-Defru¹, R. Cloutier^{2,3}, S. X. Wang⁴, J. Teske^{4,5}, R. Brahm^{6,7,8}, C. Hellier⁹, G. Ricker¹⁰, R. Vanderspek¹⁰, D. Latham², S. Seager¹¹, J. N. Winn¹², J. M. Jenkins¹³, K. A. Collins², K. G. Stassun¹⁴, C. Ziegler¹⁵, J. M. Almenara¹⁶, D. R. Anderson^{9,17}, E. Artigau¹⁸, X. Bonfils¹⁶, F. Bouchy¹⁹, C. Briceño²⁰, R. P. Butler²¹, D. Charbonneau², D. M. Conti²², J. Crane⁴, I. J. M. Crossfield^{23,24}, M. Davies¹³, X. Delfosse¹⁶, R. F. Díaz^{25,26}, R. Doyon¹⁸, D. Dragomir²⁷, J. D. Eastman², N. Espinoza²⁸, Z. Essack¹¹, F. Feng²¹, P. Figueira^{29,42}, T. Forveille¹⁶, T. Gan³¹, A. Glidden¹⁰, N. Guerrero¹⁰, R. Hart³², Th. Henning³³, E. P. Horch³⁴, G. Isopi³⁵, J. S. Jenkins³⁶, A. Jordán^{37,8}, J. F. Kielkopf³⁸, N. Law³⁹, C. Lovis¹⁹, F. Mallia³⁵, A. W. Mann³⁹, J. R. de Medeiros⁴⁰, C. Melo²⁹, R. E. Mennickent³⁰, L. Mignon¹⁶, F. Murgas¹⁶, D. A. Nusdeo⁴¹, F. Pepe¹⁹, H. M. Relles², M. Rose¹³, N. C. Santos^{42,43}, D. Ségransan¹⁹, S. Shectman⁴, A. Shporer¹⁰, J. C. Smith^{44,13}, P. Torres⁶, S. Udry¹⁹, J. Villaseñor⁴⁵, J. G. Winters², and G. Zhou²

(Affiliations can be found after the references)

ABSTRACT

We report the detection of a transiting super-Earth-sized planet ($R=1.39\pm 0.09 R_{\oplus}$) in a 1.4-day orbit around L 168-9 (TOI-134), a bright MIV dwarf ($V=11$, $K=7.1$) located at $25.15\pm 0.02 pc$. The host star was observed in the first sector of the Transiting Exoplanet Survey Satellite (TESS) mission and, for confirmation and planet mass measurement, was followed up with ground-based photometry, seeing-limited and high-resolution imaging, and precise radial velocity (PRV) observations using the HARPS and Magellan/PFS spectrographs. Combining the TESS data and PRV observations, we find the mass of L 168-9 b to be $4.60\pm 0.56 M_{\oplus}$, and thus the bulk density to be $1.74^{+0.44}_{-0.33}$ times larger than that of the Earth. The orbital eccentricity is smaller than 0.21 (95% confidence). This planet is a Level One Candidate for the TESS Mission's scientific objective – to measure the masses of 50 small planets – and is one of the most observationally accessible terrestrial planets for future atmospheric characterization.

Key words. stars: individual: L 168-9, TOI-134, TIC234994474 – stars: planetary systems – stars: late-type – technique: transits, radial velocities

1. Introduction

The best planets for detailed characterization are transiting planets, first and foremost because they allow for the possibility of unambiguous mass measurement (e.g., HD209458b Charbonneau et al. 2000; Mazeh et al. 2000; Henry et al. 2000). From the Doppler effect we can determine the minimum mass of the planet ($m \sin i$), and from the transit light curve we can determine the planetary radius and the orbital inclination (i), thus yielding a measurement of the planet's mass. Moreover, from this combination we can calculate the planet's mean density, and shed light on its internal structure by comparison with models containing different amount of iron, silicates, water, hydrogen, and helium. Furthermore, transiting planets are unique because of the feasibility to characterize the upper atmosphere by spectroscopy during transits and occultations of a significant number of planets. The forthcoming *James Webb Space Telescope* (JWST, Gardner et al. 2006) and the *Extremely Large Telescope* (ELT, de Zeeuw et al. 2014) will have unprecedented capabilities

for detailed studies of the atmospheres of terrestrial planets, and the interpretation of the results will require an accurate mass measurement (e.g., Batalha et al. 2019).

The Transiting Exoplanet Survey Satellite (TESS) (Ricker et al. 2015) started scientific operations in July 2018, aiming to detect transiting planets around bright and nearby stars – bright enough for Doppler mass measurement to be feasible. For this task, TESS surveys about 85% of the sky during the Prime Mission. The survey covering the southern ecliptic hemisphere is now complete, and the northern survey is underway. Each hemisphere is divided into 13 rectangular sectors of $96^{\circ} \times 24^{\circ}$ each. Each sector is continuously observed for an interval of 27-days, with a cadence of 2 minutes for several hundred thousand pre-selected stars deemed best suited for planet searching. Additionally, during the TESS Prime Mission, the Full Frame Images – the full set of all science and collateral pixels across all CCDs of a given camera – are available with a cadence of 30 minutes. M dwarfs are of special interest because the transit and radial-velocity signals of a given type of planet are larger for these low-mass stars than they are for Sun-like stars. In addition, compared to hotter stars M dwarfs present better conditions for the detection of planets orbiting the circumstellar habitable zone: less time consuming, larger Doppler signals, and an increased transit probability. Sullivan et al. (2015) anticipated that from 556 small ($<2R_{\oplus}$) transiting planets discovered by TESS, 23% of them will be detected orbiting bright ($K_S < 9$) stars, and that 75% of small planets will be found around M dwarfs.

* Partially based on observations made with the HARPS instrument on the ESO 3.6 m telescope under the program IDs 198.C-0838(A), 0101.C-0510(C), and 1102.C-0339(A) at Cerro La Silla (Chile).

** Data (Tables XXX) are only available at the CDS via anonymous ftp to cdsarc.u-strasbg.fr (130.79.128.5)

or via
<http://cdsarc.u-strasbg.fr/viz-bin/qcat?J/A+A/XXX/XXX>

*** This paper includes data gathered with the 6.5 meter Magellan Telescopes located at Las Campanas Observatory, Chile.

Table 1. L 168-9 (TIC 234994474) properties. Superscripts indicate the reference.

Parameter	Units	Value	Reference
R.A.	[J2000]	23 ^h 20 ^m 07.52 ^s	Gaia2018
Decl.	[J2000]	-60°03′54.64″	Gaia2018
Spectral type		M1V	Ga2014
B	[mag]	12.45±0.19	Ho2000
V	[mag]	11.02±0.06	Ho2000
B _A	[mag]	12.460±0.025	He2016
V _A	[mag]	11.005±0.018	He2016
g _A	[mag]	11.752±0.032	He2016
r _A	[mag]	10.416±0.028	He2016
i _A	[mag]	9.675	He2016
W ₁	[mag]	6.928±0.060	Cu2013
W ₂	[mag]	6.984±0.020	Cu2013
W ₃	[mag]	6.906±0.016	Cu2013
W ₄	[mag]	6.897±0.074	Cu2013
T		9.2298±0.0073	St2018
J		7.941±0.019	Cu2003
H		7.320±0.053	Cu2003
K _s		7.082±0.031	Cu2003
B _p		11.2811±0.0016	Gaia2018
G		10.2316±0.0008	Gaia2018
R _p		9.2523±0.0011	Gaia2018
π	[mas]	39.762±0.038	Gaia2018
Distance	[pc]	25.150 ± 0.024	Gaia2018
μ _α	[mas/yr]	-319.96±0.10	Gaia2018
μ _δ	[mas/yr]	-127.78±0.12	Gaia2018
dv _r /dt	[m/s/yr]	0.06865±0.00011	this work
M _s	[M _⊙]	0.62±0.03	Ma2019
R _s	[R _⊙]	0.600 ± 0.022	Sect. 2.1
T _{eff}	[K]	3800±70	Sect. 2.1
L _s	[L _⊙]	0.0673±0.0024	Sect. 2.1
log(g)	[g/cm ⁻³]	4.04±0.49	Sect. 2.1
[Fe/H]		0.04±0.17	Ne2014
log(R' _{HK})		-4.562±0.043	As2017A
P _{rot}	[days]	29.8 ± 1.3	Sect. 4.1

Reference notes: Gaia2018 – Gaia Collaboration (2018); Ga2014 – Gaidos et al. (2014); Ho2000 – Høg et al. (2000); H22016 – Henden et al. (2016); Cu2013 – Cutri & et al. (2013); St2018 – Stassun et al. (2018b); Cu2003 – Cutri et al. (2003); Ma2019 – Mann et al. (2019); Ne2014 – Neves et al. (2014); As2017a – Astudillo-Defru et al. (2017a)

This paper reports the discovery of a small planet orbiting the star L 168-9 (TOI-134), based on TESS data. The host star is a bright M dwarf. An intense precise radial-velocity campaign with HARPS and the Planet Finder Spectrograph (PFS) revealed the terrestrial nature of the newly detected world. This work is presented as follows: Section 2 describes the host star properties. Sections 3.1 and 3.3 describe the photometric and radial-velocity observations. Section 4 presents an analysis of all the data, including the study of stellar activity. Finally, Section 6 places L 168-9 b within the larger context of the sample of detected planets.

2. L 168-9

L 168-9, also known as CD-60 8051, HIP 115211, 2MASS J23200751-6003545, with the entry 234994474 of the TESS Input Catalog (TIC) or 134 of the Tess Object of Interest (TOI) list, is a red dwarf of spectral type M1V. It appears in the southern sky, and resides at a distance of 25.150±0.024

pc from the Sun (Gaidos et al. 2014; Gaia Collaboration 2018). Table 1 lists the key parameters of the star, namely its position, visual and near-infrared apparent magnitudes, parallax, proper motion, secular acceleration, and its essential physical properties.

2.1. Derived stellar properties

We performed an analysis of the broadband spectral energy distribution (SED) together with the *Gaia* DR2 parallax in order to determine an empirical measurement of the stellar radius, following the procedures described by Stassun & Torres (2016); Stassun et al. (2017, 2018a). We took the $B_T V_T$ magnitudes from *Tycho-2*, the $B_V g_{ri}$ magnitudes from APASS, the JHK_S magnitudes from 2MASS, the W1–W4 magnitudes from *WISE*, and the G magnitude from *Gaia*. Together, the available photometry spans the full stellar SED over the wavelength range 0.35–22 μm (see Figure 1).

We performed a fit using NextGen stellar atmosphere models (Hauschildt et al. 1999), with the effective temperature (T_{eff}) and surface gravity ($\log g$) constrained on the ranges reported in the TESS Input Catalog (Stassun et al. 2018b), while the metallicity [Fe/H] was fixed to a typical M-dwarf metallicity of -0.5. We fixed the extinction (A_V) to be zero, considering proximity of the star, the degrees-of-freedom of the fit is 10. The resulting fit (Figure 1) has a χ^2 of 42.3 ($\chi^2_{\text{red}}=4.2$), with $T_{\text{eff}} = 3800 \pm 70$ K. The relatively high χ^2 is likely due to systematics, as the stellar atmosphere model is not perfect. We artificially increased the observational uncertainty estimates until $\chi^2_{\text{red}} = 1$ was achieved. Integrating the (unreddened) model SED gives the bolometric flux at Earth of $F_{\text{bol}} = 3.41 \pm 0.12 \times 10^{-9}$ erg s⁻¹ cm⁻². Taking the F_{bol} and T_{eff} together with the *Gaia* DR2 parallax, adjusted by +0.08 mas to account for the systematic offset reported by Stassun & Torres (2018), gives the stellar radius as $R = 0.600 \pm 0.022 R_{\odot}$. Finally, estimating the stellar mass from the empirical relations of Mann et al. (2019) gives $M = 0.62 \pm 0.03 M_{\odot}$. With these values of the mass and radius, the stellar mean density is $\rho = 4.04 \pm 0.49$ g cm⁻³. We also tested to fit the SED using BT-Settl theoretical grid of stellar model (Allard 2014), where we obtained a consistent result.

We searched for infrared (IR) excess in *WISE* data using the Virtual Observatory SED Analyser (VOSA, Bayo et al. 2008), which could point for the presence of debris disks. For that we computed the excess significance parameter (χ_{λ} , Beichman et al. 2006; Moór et al. 2006), where $\chi_{\lambda} \geq 3$ represents a robust detection of IR excess. We obtained $\chi_{\lambda} = 0.70$ in the W₃ band, ruling out the presence of a debris disk around L 168-9.

3. Observations

The first hint of a planetary companion orbiting L 168-9 came from analyzing TESS data. After the Data Validation Report was released to the community, a follow-up campaign started with several instruments and by different teams to check on whether the transit-like signal seen by TESS originated from a planet, as opposed to a stellar binary or other source. The follow-up observations included supplementary time series photometry aiming to detect additional transits, seeing-limited and high-resolution imaging to analyze the possibility that the signal comes from a star on a nearby sightline, and precise radial-velocity monitoring to measure the companion’s mass.

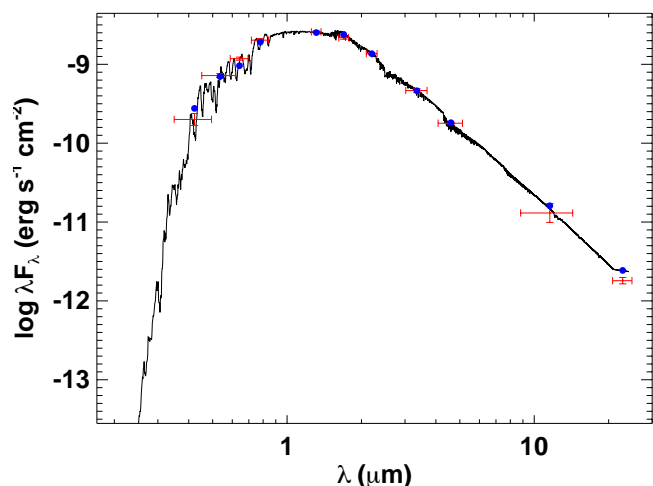


Fig. 1. Spectral energy distribution (SEDs) of L 168-9. Red error bars represent the observed photometric measurements, where the horizontal bars represent the effective width of the passband. Blue circles are the model fluxes from the best-fit NextGen atmosphere model (black).

3.1. Photometry

3.1.1. TESS

TESS observed Sector 1 from the 25th of July to the 22nd of August 2018¹, a 27.4-day interval that is typical of each sector. L 168-9 is listed in the Cool Dwarf Catalog that gathered the known properties of as many dwarf stars as possible with $V - J > 2.7$ and effective temperatures lower than 4000 K (Muirhead et al. 2018). The predicted TESS-band apparent magnitudes are also given in this catalog. L 168-9 was chosen for 2-min time sampling as part of the TESS Candidate Target List (CTL, Stassun et al. 2018b), consisting of a subset of the TESS Input Catalog (TIC) identified as high-priority stars in the search for small transiting planets. Time series observations of L 168-9 were made with CCD 2 of Camera 2.

The TESS Science Processing Operations Center (SPOC) at the NASA Ames Research Center performed the basic calibration, reduction, and de-trending of the time series, and also performed the search for transit-like signals (Jenkins et al. 2016). The light curves were derived by the SPOC pipeline and consist of a time series based on Simple Aperture Photometry (SAP), as well as a corrected time series based on Pre-search Data Conditioning (PDC, Smith et al. 2012; Stumpe et al. 2014) referred to as PDCSAP (as detailed by Tenenbaum and Jenkins 2018²). This work made use of the PDCSAP time series available on the Mikulski Archive for Space Telescopes (MAST³). The TESS photometry is presented in the upper panel in Figure 6.

A Data Validation Report for L 168-9 was released to the community as part of the MIT TESS Alerts⁴. The report includes several validation tests to assess the probability that the signal is a false positive: eclipsing-binary discrimination tests, a statistical bootstrap test, a ghost diagnostic test, and difference-image centroid offset tests. These are described by Twicken et al. (2018). All the tests were passed successfully. The formal false-

alarm probability of the planet candidate was reported to be 5.85×10^{-37} .

The TESS time series covers 19 transits of what was originally deemed a planet candidate (L 168-9 b or TOI-134.01), and reported on the TESS exoplanet Follow-up Observing Program (TFOP) website⁵. According to the Data Validation Report the orbital period is $P = 1.401461 \pm 0.000137$ days and the transit depth is $\Delta F/F_0 = 566 \pm 38$ ppm, which translates into a planetary radius of $R_p = 1.58 \pm 0.36 R_\oplus$ (Sect. 2.1 describes how we determined the stellar radius, which is the same value as the used in the Validation Report). The time of mid-transit at an arbitrarily chosen reference epoch is (BJD) $T_c = 2458326.0332 \pm 0.0015$.

3.1.2. LCOGT, MKO, and SSO T17

We acquired ground-based time series photometric follow-up of L 168-9 and the nearby field stars as part of the TESS Follow-up Observing Program (TFOP) to attempt to rule out nearby eclipsing binaries (NEBs) in all stars that are bright enough to cause the TESS detection and that could be blended in the TESS aperture. We used the TESS Transit Finder⁶, which is a customized version of the Tapir software package (Jensen 2013), to schedule our transit observations.

We observed one full transit simultaneously using three 1-meter telescopes at the Las Cumbres Observatory Global Telescope (LCOGT) (Brown et al. 2013) South Africa Astronomical Observatory node on 21 September 2018 in i' -band. The Sinistro detectors consist of $4K \times 4K$ $15\text{-}\mu\text{m}$ pixels with an image scale of $0\text{'}.389$ pixel⁻¹, resulting in a field-of-view of $26\text{'}.5 \times 26\text{'}.5$. The images were calibrated by the standard LCOGT BANZAI pipeline.

We observed a full transit from the Mount Kent Observatory (MKO) 0.7-meter telescope near Toowoomba, Australia on 23 September 2018 in r' -band. The Apogee U16 detector consists of $4K \times 4K$ $9\text{-}\mu\text{m}$ pixels with an image scale of $0\text{'}.41$ pixel⁻¹, resulting in a field-of-view of $27\text{'}.0 \times 27\text{'}.0$. The images were calibrated using AstroImageJ (AIJ) software package (Collins et al. 2017).

We observed a full transit from the Siding Spring Observatory, Australia, iTelescope T17 0.43-meter telescope on 27 September 2018 with no filter. The FLI ProLine PL4710 detector consists of $1K \times 1K$ pixels with an image scale of $0\text{'}.92$ pixel⁻¹, resulting in a field-of-view of $15\text{'}.5 \times 15\text{'}.5$. The images were calibrated using AstroImageJ.

We used the AstroImageJ to extract differential light curves of L 168-9 and all known stars within $2\text{'}.5$ of the target star that are bright enough to have possibly produced the shallow TESS detection, which includes 11 neighbors brighter than TESS-band = 17.9 mag. This allows an extra 0.5 in delta magnitude relative to L 168-9 to account for any inaccuracies in the TESS band reported magnitudes in the TICv8. The L 168-9 light curves in all five photometric data sets show no significant detection of the shallow TESS detected event, as expected from our lower precision ground-based photometry. Considering a combination of all five photometric data sets, we exclude all 11 known neighbors that are close enough and bright enough to L 168-9 to have possibly caused the TESS detection as potential sources of the TESS detection.

¹ The Sector 1 pointing direction was $RA(J2000) : +352.68^\circ$, $Dec(J2000) : -64.85^\circ$, $Roll : -137.85^\circ$.

² <https://archive.stsci.edu/missions/tess/doc/EXP-TESS-ARC-ICD-TM-0014.pdf>

³ <https://mast.stsci.edu/portal/Mashup/Clients/Mast/Portal.html>

⁴ <https://tev.mit.edu/toi/alerts/>

⁵ <https://exofop.ipac.caltech.edu/tess/>

⁶ https://astro.swarthmore.edu/telescope/tess-secure/find_tess_transits.cgi

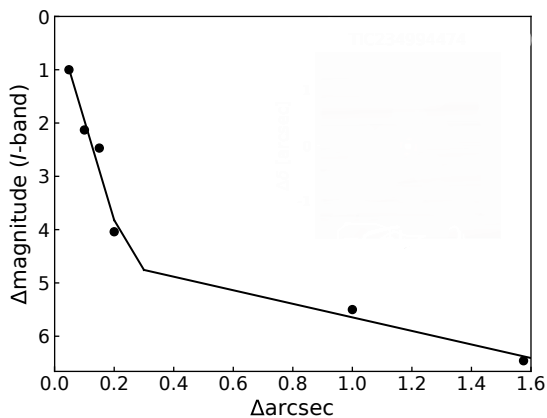


Fig. 2. SOAR speckle results of L 168-9. Black points represent the I-band contrast obtained at a given separation of the star. The solid black line shows the 5σ detection limit curve.

3.1.3. WASP

WASP-South, located in Sutherland, South Africa, is the southern station of the *Wide Angle Search for Planets* (WASP, Pol-lacco et al. 2006). It consists of an array of 8 cameras each backed by a 2048x2048 CCD. Observations in 2010 and 2011 (season A) used 200mm, f/1.8 lenses with a broadband filter spanning 400 – 700 nm and a plate scale of $13.7''/\text{pixel}$. Then, from 2012 to 2014 (season B), WASP-South used 85mm, f/1.2 lenses with a Sloan r' filter and a plate scale of $32''/\text{pixel}$. The array rastered a number of fields each clear night at typically 10-min cadence.

L 168-9 was monitored for four consecutive years, from to May 20, 2010 to December 12, 2014; typically covering 150 days in each year. In one campaign two cameras with overlapping fields observed the star, giving a total of 27 300 data points; in another campaign, L 168-9 was observed by three cameras with overlapping fields, totalling 170 000 data points. The photometry has a dispersion of $0.027 \delta\text{mag}$ and average uncertainty of $0.024 \delta\text{mag}$, presenting clear signs of variability, as shown below in Sec. 4.1.

3.2. High-resolution Imaging

The relatively large $21''$ pixels of TESS can lead to photometric contamination from nearby sources. These must be accounted for to rule out astrophysical false positives, such as background eclipsing binaries, and to correct the estimated planetary radius, initially derived from the diluted transit in a blended light curve (Ziegler et al. 2018). Without this correction, the interpreted planet radius can be underestimated (e.g., Ciardi et al. 2015; Teske et al. 2018).

3.2.1. SOAR

We searched for close companions to L 168-9 with speckle imaging on the 4.1-m Southern Astrophysical Research telescope (SOAR, Tokovinin 2018) installed in Cerro Pachón, Chile, on 2018 September 25 UT using the I-band ($\lambda_{cen} = 824 \text{ nm}$, full width at half maximum = 170 nm) centered approximately on the TESS passband. Further details of the TESS SOAR survey are published in Ziegler et al. (2019).

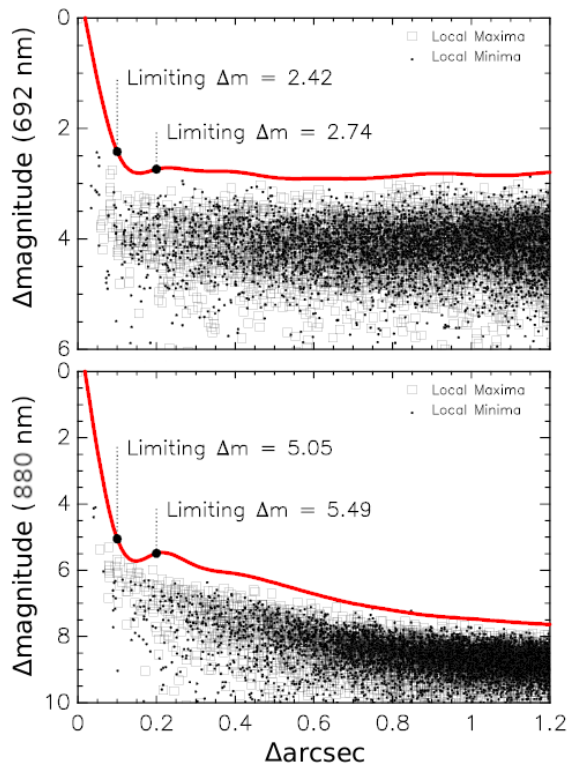


Fig. 3. DSSI/Gemini-S detection limit curves of L 168-9 in the 692 nm (top) and 880 nm (bottom) filters. Squares and points on left panel represent local maxima and local minima, respectively.

Figure 2 shows the 5σ detection sensitivity. No nearby stars ($\rho < 1''/6$) to L 168-9 were detected within the sensitivity limits of SOAR.

3.2.2. Gemini-South

Observations of L 168-9 were conducted with the Differential Speckle Survey Instrument (DSSI; Horch et al. 2009) on Gemini South, Chile, on UT 28 October 2018 under program GS-2018B-LP-101 (PI: I. Crossfield). The usual 692 nm and 880 nm filters on DSSI were used, and three sequences of $60 \text{ ms/frame} \times 1000$ frames were taken. The total time on target, including readout overhead, was six minutes. Howell et al. (2011), Horch et al. (2011), and Horch et al. (2012) detail the speckle observing and data reduction procedures. The detection limit curves are shown in Figure 3. While the 692 nm image was taken at too low of gain, leading to a shallow detection limit, the 880 nm detection limit curve (b) in Figure 3 indicates that L 168-9 lacks any companions of $\Delta m \sim 5.0 \text{ mag}$ beyond $0.1''$ and any companions of $\Delta m \sim 5.5 \text{ mag}$ beyond $0.2''$. Gemini-South and SOAR result (Sect. 3.2.1) mean the transit signal is likely to be associated with L 168-9.

Thus, we conclude that there is no significant contamination of the TESS photometric aperture that would bias the determination of the planet radius. The Sinistro data (Sect. 3.1.2) rule out surrounding stars as potential sources of the TESS detection, so we can assume the planet orbits L 168-9. Given the limits placed on nearby companions by the Gemini-South data, if there were a close companion it would have to be fainter by ~ 5 magnitudes than the primary star, meaning the planet radius correction factor would be at most

$$R_{p,corr} = R_p \times \sqrt{1 + 10^{-0.4\Delta m}} = R_p \times 1.005. \quad (1)$$

This is smaller than the derived planet radius uncertainty (Table 2).

3.3. Radial velocity

3.3.1. HARPS

The *High Accuracy Radial velocity Planet Searcher* (HARPS Mayor et al. 2003) is an echelle spectrograph mounted on the 3.6m telescope at La Silla Observatory, Chile. The light is spread over two CCDs (pixel size $15\ \mu\text{m}$) by a science fiber and a calibration fiber. The calibration fiber can be illuminated with the calibration lamp for the best radial velocity precision, or it can be placed on sky for moderate precision. HARPS is stabilized in pressure and temperature, and has a resolving power of 115,000. The achievable precision in radial velocity of better than $1\ \text{m/s}$.

We began monitoring L 168-9 with HARPS on September 29, 2018, soon after the TESS alert. We elected not to use the simultaneous wavelength calibration (i.e. the on-sky calibration fiber) to ensure that the bluer spectral regions would not be contaminated by the calibration lamp, that provides a much stronger flux for any instrumental setup. The exposure time was set to 900 s for ESO programs 198.C-0838 and 1102.C-0339, and to 1,200 s for ESO program 0101.C-0510, translating in a median signal-to-noise ratio per spectral pixel of 51 and 70 at 650 nm, respectively. A single spectrum on October 1, 2018, had an exposure time of 609 s for an unknown reason. A total of 47 HARPS spectra were collected, ending with observations on December 19, 2018.

HARPS spectra were acquired in roughly three packs of data separated in time by about 40 days. This sampling is reflected in the window function presented in Figure 5. Two archival spectra of L 168-9 are available at the ESO database. However, a radial velocity offset was introduced on May 2015 because the vacuum vessel was opened during a fiber upgrade (Lo Curto et al. 2015). As this offset is not yet well characterized for M dwarfs, we decided to disregard those two points (from July 2008 and June 2009) in our subsequent analysis.

The HARPS Data Reduction Software (Lovis & Pepe 2007) computes radial velocities by a cross-correlation function technique (Baranne et al. 1996, e.g.). Nevertheless we derived radial velocities by a different approach to exploit as much as possible the Doppler information of spectra (e.g., Anglada-Escudé & Butler 2012). We performed a maximum likelihood analysis between a stellar template and each individual spectrum following the procedure presented in Astudillo-Defru et al. (2017c). The stellar template corresponds to a true stellar spectrum of the star, enhanced in signal-to-noise. It was made from the median of all the spectra, after shifting them into a common barycentric frame. The resulting template is Doppler shifted by a range of trial radial velocities to construct the maximum likelihood function, from which we derived the HARPS radial velocity used in the subsequent analysis. The obtained radial velocities – listed in Table B.1 – present a dispersion of $4.01\ \text{m/s}$ and a median photon uncertainty of $1.71\ \text{m/s}$. Figure 7 shows the radial velocities folded to the orbital period.

3.3.2. PFS

The Planet Finder Spectrograph is an iodine-calibrated, environmentally controlled high resolution PRV spectrograph (Crane et al. 2006, 2008, 2010). Since first light in October 2009, PFS has been running a long-term survey program to search for planets around nearby stars (e.g., Teske et al. 2016). In January 2018,

PFS was upgraded with a new large format CCD with $9\ \mu\text{m}$ pixels and switched to a narrower slit for its regular operation mode to boost the resolution from 80,000 to 130,000. The PFS spectra are reduced and analyzed with a custom IDL pipeline that is capable of delivering RVs with $<1\ \text{m/s}$ precision (Butler et al. 1996).

We followed up L 168-9 with PFS on the 6.5 m Magellan II Clay telescope at Las Campanas Observatory in Chile from October 13–26, and then on December 16 and 21 in 2018. Observations were conducted on 15 nights, with multiple exposures per night. There were a total of 76 exposures of 20 minutes each. We typically took 2–6 exposures per night over a range of timescales, to increase the total SNR per epoch and also to average out the stellar and instrumental jitter. Each exposure had a typical SNR of 28 per pixel near the peak of the blaze function, or 56 per resolution element. The radial velocity dispersion is $4.61\ \text{m/s}$ and the median RV uncertainty per exposure is about $1.8\ \text{m/s}$. Five consecutive 20-minute iodine-free exposures were obtained to allow for the construction of a stellar spectral template in order to extract the RVs. These were bracketed with spectra of rapidly rotating B stars taken through the iodine cell, for reconstruction of the spectral line spread function and wavelength calibration for the template observations.

The PFS observations of L 168-9 presented here are part of the Magellan TESS Survey (MTS) that will follow up ~ 30 super-Earths and sub-Neptunes discovered by TESS in the next three years using PFS (Teske et al. in prep.). The goal of MTS is to conduct a statistically robust survey to understand the formation and evolution of super-Earths and sub-Neptunes. The observation schedules of all MTS targets, including L 168-9, can be found on the ExoFOP-TESS website.⁷

4. Analysis

4.1. Photometric rotation period

Knowledge of the stellar rotation period helps to disentangle spurious RV signals arising from rotation and true RV signals due to orbital motion (e.g., Queloz et al. 2001; Cloutier et al. 2017). L 168-9 was photometrically monitored by WASP between May 2010 and December 2014 within five observing seasons each lasting approximately 200 days in duration. The photometric precision, observing cadence, and baselines within the WASP fields are sufficient to detect quasi-periodic (QP) photometric variations of L 168-9 due to active regions on the stellar surface rotating in and out of view at the stellar rotation period P_{rot} . The WASP photometry of L 168-9 is shown in Fig. 4 along with the generalized Lomb-Scargle periodogram (GLSP; Zechmeister & Kürster 2009) of the photometry in each of the five WASP observing seasons. It is clear from the GLSPs that a strong periodicity exists within the data whose timescale is often ~ 30 days except for within the second WASP season wherein the dominant periodicity appears at the first harmonic of $P_{\text{rot}} \sim 15$ days.

Given periodicities significantly detected in the WASP photometry, we proceeded to measure the photometric rotation period of L 168-9 P_{rot} with each WASP camera and in each WASP field⁸ in which L 168-9 was observed. As the photometric variations appear to vary nearly periodically, we modeled the photometry with a Gaussian process (GP) regression model and

⁷ <https://exofop.ipac.caltech.edu/tess/>

⁸ At times, L 168-9 appeared within the fields-of-view of multiple WASP cameras.

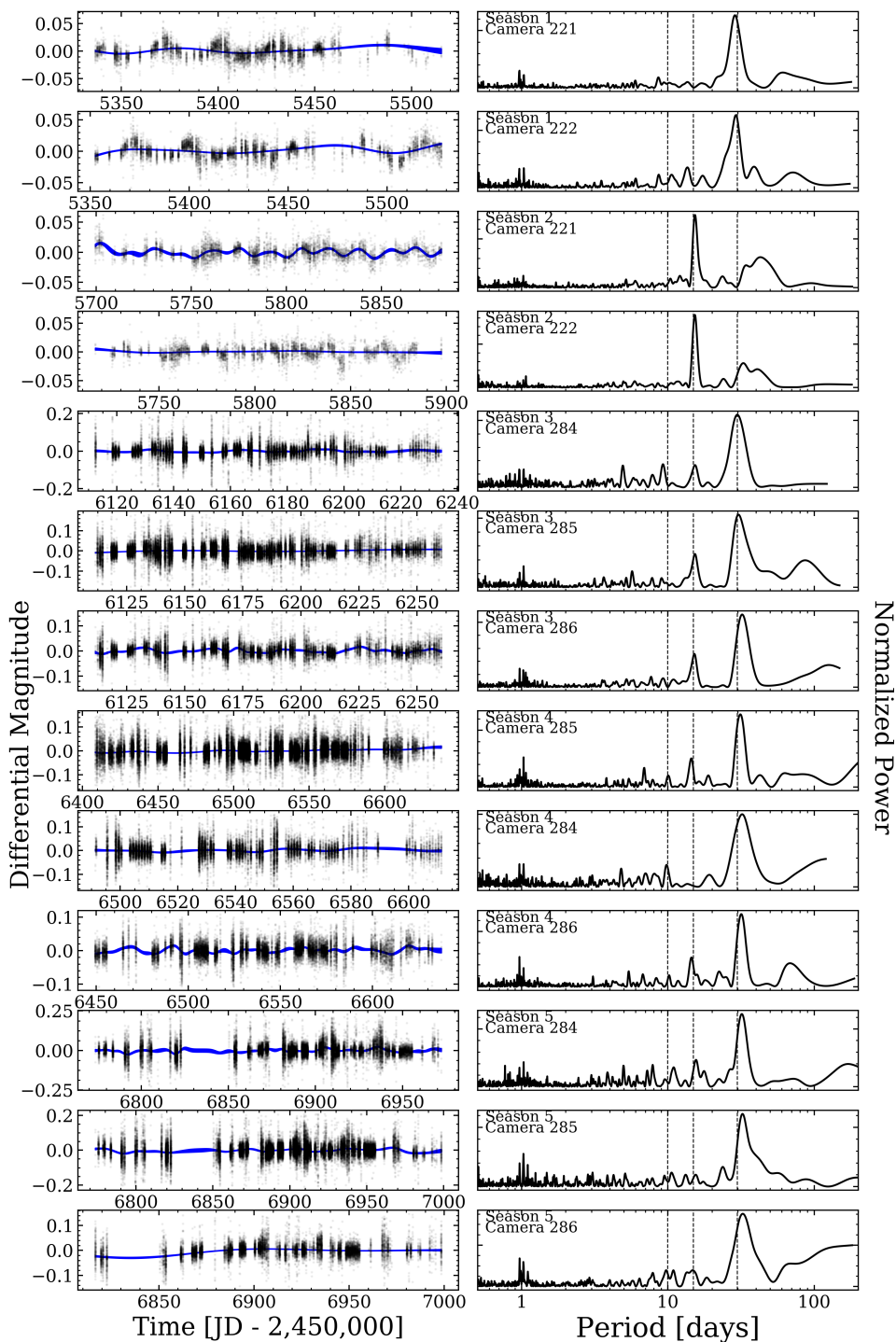


Fig. 4. The WASP photometry. *Left column:* The photometry time series; the blue shaded regions depict $\pm 1\sigma$ about the mean GP regression model of the binned photometry. *Right column:* the generalized Lomb-Scargle periodogram of each season highlights the prevalence of photometric variations close to the measured rotation period and/or its first and second harmonics (vertical dashed lines).

adopted a QP covariance kernel (see Eq. A.1) (Angus et al. 2018). The covariance function’s periodic timescale was a free parameter P_{rot} for which the posterior probability density function (PDF) was sampled using a Markov Chain Monte Carlo (MCMC) method (see Appendix A). We modeled each binned WASP light curve with a GP. We adopted a bin size of 1 day to reduce the computation time. In preliminary analyses, we also tested bin sizes of 0.25, 0.5, and 2 days and found that, probably due to the very large number of points, the recovered values of P_{rot} were not very sensitive to this choice.

After sampling the posterior PDFs of the GP hyperparameters, we arrived at point estimates of each parameter value based on the maximum a-posteriori values and 68 percent confidence

intervals. The resulting mean GP model of the data from each WASP observing season is depicted in Fig. 4 along with the corresponding 1σ confidence interval. Over the five observing seasons, the measured (median) rotation period of L 168-9 was $P_{\text{rot}} = 29.8 \pm 1.3$ days.

In principle, the WASP signal could have arisen from any star within the $48''$ extraction aperture. However, L 168-9 is by far the brightest star in the aperture. Another concern with any photometric signal with a period near 30 days is whether it was affected by moonlight. To check on this possibility, we searched for modulations in the WASP data of several stars of similar brightness within the surrounding 10 arcmin field, but did not find any 30-d signals similar to the one that was seen

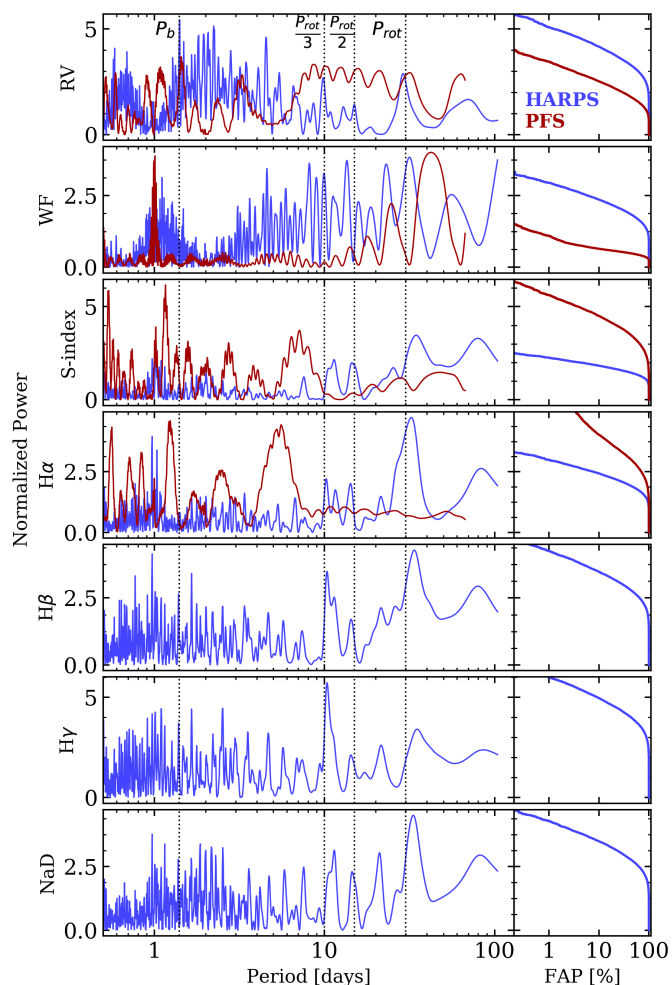


Fig. 5. *Left column:* Generalized Lomb-Scargle periodograms of the HARPS and PFS RV time series, window functions, and the S-index, $H\alpha$, $H\beta$, $H\gamma$, and sodium doublet activity indicators. The vertical dotted lines highlight the locations of the L 168-9 b orbital period, the stellar rotation period, and its first two harmonics. *Right column:* the false alarm probabilities computed from bootstrapping with replacement.

for L 168-9. In any case, the star location is far from the ecliptic, and moonlight contamination is not expected. Furthermore, the modulation was sometimes seen at the 15-d first harmonic, which would not be expected for moonlight. We can therefore be confident that the 30-d periodicity in the WASP data arises from L 168-9. The R'_{HK} from HARPS spectra supports the obtained photometric rotation period, as $\log(R'_{HK}) = -4.562 \pm 0.043$ (active star) translates into $P_{\text{rot}} = 22 \pm 2$ days using the R'_{HK} vs. P_{rot} relationship from Astudillo-Defru et al. (2017a).

4.2. Radial Velocity Periodogram Analysis

A first identification of significant periodicities in the HARPS and PFS RV time series is required in order to develop an accurate model of the observed RV variations. In a manner similar to our analysis of the WASP photometry, we computed the GLSP of the following HARPS and PFS spectroscopic time series: the RVs, the window functions (WF), and the S-index, $H\alpha$, $H\beta$, $H\gamma$, and the sodium doublet NaD activity indicators. Astudillo-Defru et al. (2017c) details how these spectroscopic activity indicators were derived. Each GLSP is shown in Fig. 5 along with a false alarm probability (FAP) that was computed via bootstrap-

ping with replacement using 10^4 iterations and normalizing each periodogram by its standard deviation.

Each of the GLSPs of the HARPS and PFS RV time series is dominated by noise and aliases arising from the respective WF. For example, the HARPS WF contains a forest of peaks with comparable FAP from ~ 8 days and extending out towards long periodicities. Similarly the GLSP of the PFS WF reveals a series of broad peaks for periodicities ≥ 1 day. These features, particularly those from the PFS WF, have clear manifestations in the GLSPs of their respective RV and activity indicator time series, thereby complicating the robust identification of periodicities in the data. However, strong peaks at the orbital period of L 168-9 b (~ 1.4 days) are discernible in both RV time series at FAP $\sim 0.4\%$ and $\sim 0.3\%$ with HARPS and PFS respectively. This periodicity is not apparent in any of the ancillary activity indicators time series as expected for a signal originating from an orbiting planet.

In addition to the signal from L 168-9 b, the HARPS RVs exhibit some power close to P_{rot} and its second harmonic $P_{\text{rot}}/3$. Although the FAPs of these periodicities over the full frequency domain are large, they each appear locally as strong periodicities as most of the power in the HARPS RVs exists at $\lesssim 5$ days. The GLSP of the PFS RVs is much more difficult to interpret at periodicities in the vicinity of P_{rot} and its first and second harmonics due to strong aliases from the PFS WF. Due to these effects it is difficult to discern from the available PFS activity indices (i.e. S-index and $H\alpha$) whether or not a coherent activity signal is seen with PFS. Although each of the HARPS and PFS RV time series are significantly affected by sampling aliases, we do see evidence for L 168-9 b and rotationally modulated stellar activity in the RVs we endeavor to mitigate with our adopted model discussed in Sect. 4.3.

4.3. Radial velocity + transit model

Guided by the periodicities in the HARPS and PFS RV time series, we proceeded to fit a model to the RVs including the effects of both stellar activity and the planet. Following numerous successful applications on both Sun-like (e.g., Haywood et al. 2014; Grunblatt et al. 2015; Faria et al. 2016; López-Morales et al. 2016; Mortier et al. 2016) and M dwarf stars (e.g., Astudillo-Defru et al. 2017b; Bonfils et al. 2018; Cloutier et al. 2019; Ment et al. 2019), we adopted a QP kernel for the GP as a non-parametric model of the physical processes resulting in stellar activity. When used to model RV stellar activity, the QP covariance kernel is often interpreted as modelling the rotational component of stellar activity from active regions on the rotating stellar surface whose lifetimes typically exceed many rotation cycles on M dwarfs (Giles et al. 2017) plus the evolutionary time scale of the active regions. The corresponding GP hyperparameters are described in detail in Appendix A and include each spectrograph's covariance amplitudes a_{HARPS} , a_{PFS} , the common exponential timescale λ_{RV} , the common coherence parameter Γ_{RV} , and the common periodic timescale P_{RV} equal to the stellar rotation period P_{rot} .

The planetary component attributed to the transiting planet L 168-9 b was fitted to the de-trended light curve with a Mandel & Agol (2002) planetary transit model. The de-trended TESS light curve was produced by adjusting a QP GP systematic model to the photometry alone and with all the transits previously removed. The best QP GP model was subtracted to the entire TESS data set. The planetary component is modelled by a Keplerian solution parameterized by the planet's orbital period P_b , time of mid-transit T_0 , RV semi-amplitude K , and the orbital parameters

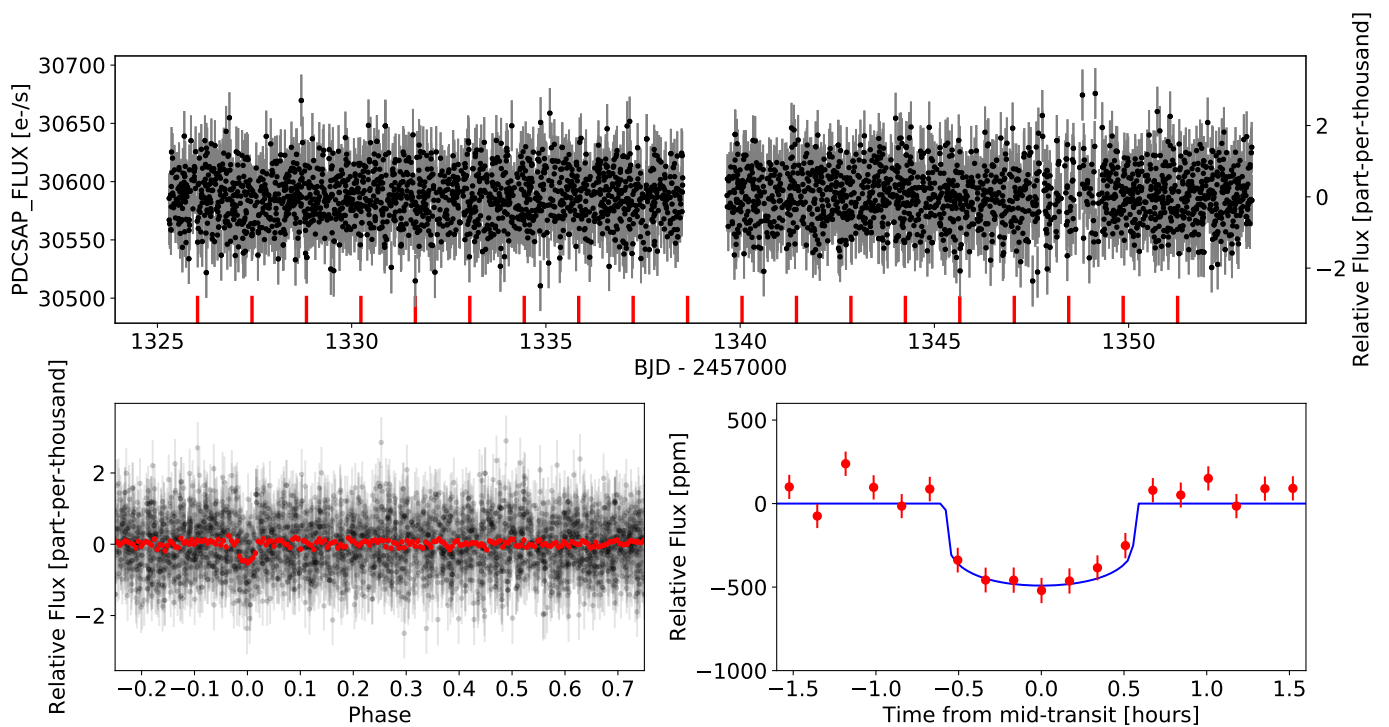


Fig. 6. The time series of TESS data for L 168-9. One fifth of original data are plotted for visualization purposes. The de-trended TESS light curve is shown in the *upper panel*. Red vertical bars represent the transits of the planet candidate. *Bottom panel*: the phase folded normalized photometry. Red points correspond to binned data for illustrative purposes. The whole orbital phase is shown to the left, while the right presents the transit phase, as well as the best transit model whose parameters come from the Table 2.

$h = \sqrt{e} \cos \omega$ and $k = \sqrt{e} \sin \omega$ where e and ω are the planet's orbital eccentricity and argument of periastron respectively. In addition, our RV model contains each spectrograph's zero point velocity γ_{HARPS} , γ_{PFS} and an additive scalar jitter s_{HARPS} , s_{PFS} is account for any residual jitter that, unlike the stellar activity signal, is not temporally correlated. The complete RV model therefore contains fourteen model parameters.

To ensure self-consistent planet solutions between the available TESS transit data and the RV observations, we simultaneously fitted the de-trended light curve and the RVs. The common planetary parameters between these two data sets are P_b , T_0 , h , and k . The additional model parameters required to model the TESS transit light curve included an additive scalar jitter s_{TESS} , the baseline flux γ_{TESS} , the scaled semi-major axis a/R_s , the planet-star radius ratio r_p/R_s , the orbital inclination i , and the nearly-uncorrelated parameters q_1 and q_2 which are related to the quadratic limb darkening coefficients u_1 and u_2 via

$$q_1 = (u_1 + u_2)^2 \quad (2)$$

$$q_2 = \frac{u_1}{2(u_1 + u_2)}. \quad (3)$$

(Kipping 2013). Thus we required eleven model parameters to describe the TESS transit light curve and a total of twenty-one model parameters of the joint RV + light curve data set: $\Theta = \{a_{\text{HARPS}}, a_{\text{PFS}}, \lambda_{\text{RV}}, \Gamma_{\text{RV}}, P_{\text{RV}}, s_{\text{TESS}}, s_{\text{HARPS}}, s_{\text{PFS}}, \gamma_{\text{TESS}}, \gamma_{\text{HARPS}}, \gamma_{\text{PFS}}, P_b, T_0, K, h, k, a/R_s, r_p/R_s, i, q_1, q_2\}$.

We sampled the posterior PDF of this 21-dimensional parameter space using an MCMC sampler. Details on the sampler and the adopted prior distributions on each model parameter are given in Appendix A and Table A.1.

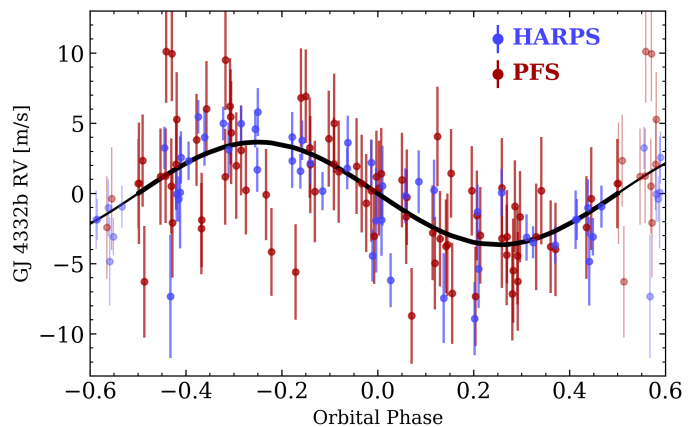


Fig. 7. Phase folded radial velocity acquired HARPS (blue points) and PFS (red points) where the best GP model was subtracted. The black curve represents the maximum a-posteriori model adjusted to the data set.

5. Results

In our analysis of the light curve and radial velocity time series of L 168-9, we evaluated the model presented in Sect. 4.3 on the separate RV data sets obtained with HARPS and PFS as well as the combined time series. Subtracting the model to the 46 HARPS radial velocity points reduces the dispersion to 3.37 m/s (equivalent to $\chi_{\text{red}}^2 = 3.5$), while the dispersion of the 76 PFS residual points gives 4.05 m/s (translating into $\chi_{\text{red}}^2 = 1.5$). The dispersion obtained from the 122 HARPS+PFS residual points is 3.80 m/s ($\chi_{\text{red}}^2 = 2.2$).

From point estimates of the model parameters Θ from our joint RV plus transit analysis with each of these input data sets we retrieved that L 168-9 b has a radius of $1.39 \pm 0.09 R_{\oplus}$ and a mass of $4.60 \pm 0.56 M_{\oplus}$, translating into a bulk mean density of $9.6^{+2.4}_{-1.8} \text{ g cm}^{-3}$. The planet is orbiting at 0.02091 ± 0.00024 AU from the parent star, therefore the hot terrestrial planet has an equilibrium temperature between 668 K and 965 K assuming a Venus-like and zero bond albedo, respectively. Results for the entire set of parameters are reported in Table 2. Explicitly, we report the maximum a-posteriori value of each parameter along with its 16th and 84th percentiles, corresponding to a 1σ confidence interval. We check for consistency of our joint analysis by performing the analysis for each instrument independently. Table 2 details the results from this test. We note that HARPS and PFS results are in agreement within their uncertainties, translating into a robust detection of the planetary signal in radial velocity data.

Figure 6 show the TESS photometry and adjusted transit model and Figure 7 the phase folded radial velocity with the model that best fits the data.

6. Discussion & Conclusions

L 168-9 b adds to the family of small ($< 2R_{\oplus}$) transiting planets around bright ($J < 8$ mag) stars with mass measurements and contributes to the completion of the TESS Level One Science Requirement to detect and measure the masses of 50 small planets. In particular, L 168-9 b is one of fourteen⁹ likely rocky planets without primordial hydrogen-helium envelopes – that is, with a radius $< 1.8R_{\oplus}$ – for which the mass has been measured with an uncertainty smaller than 33%. Thus, our result represents progress toward the understanding of the transition between super-Earths and mini-Neptunes previously reported in the radii of planets (e.g. Fulton et al. 2017; Cloutier & Menou 2019) but, here, including the information on mass.

Figure 8 shows the mass - radius diagram centered in the sub-Earth to mini-Neptune regime. With about twice the Earth average density, L 168-9 b bulk density is compatible with a terrestrial planet with an iron core (50%) surrounded by a mantle of silicates (50%). In this diagram the detected planet is located in an interesting place: for masses lower than that of L 168-9 b the great majority of planets are consistent with a 50% Fe–50% MgSiO₃ or 100% MgSiO₃ bulk composition, while for higher planetary masses there is a great diversity of density. Being one of the densest planets for masses greater than $4M_{\oplus}$, L 168-9 b can help to define the mass limits of the rocky planets population.

Good targets for atmospheric characterization with transmission/emission spectroscopy are those transiting nearby, bright stars ($J < 8$ mag). There are currently 11 small planets detected transiting a bright star, according to the NASA Exoplanet Archive¹⁰, two of them orbit M dwarfs. Overall, there would not be a large number of small, transiting planets around nearby, bright M dwarfs. There are roughly 200 M dwarfs within the 25 pc solar neighborhood with $J < 8$ mag, about 2/3 of which

⁹ L 98-59 bc (Cloutier, R. et al. 2019), GJ 357 b (Luque et al. 2019), HD 15337 b (Dumusque et al. 2019), HD 213885 b (Espinoza et al. 2019), GJ 9827 b (Rice et al. 2019), K2-265 b (Lam et al. 2018), K2-141 b (Barragán et al. 2018), K2-229 b (Santerne et al. 2018), HD 3167 b (Gandolfi et al. 2017), K2-106 b (Guenther, E. W. et al. 2017), TRAPPIST-1 fh (Wang et al. 2017), HD 219134 b (Motalebi et al. 2015)

¹⁰ <https://exoplanetarchive.ipac.caltech.edu/>

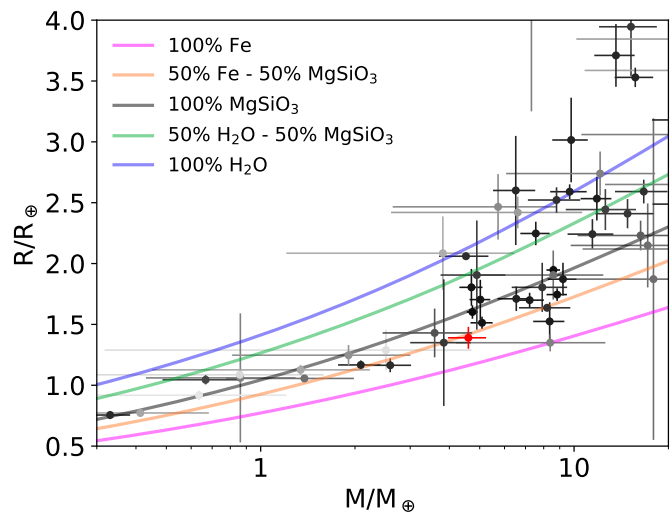


Fig. 8. The mass-radius diagram showing L 168-9 b (red circle) in the context of known exoplanets. The transparency of each point is proportional to its associated mass uncertainty. Error bars correspond to 1σ uncertainties. Different models for the bulk composition are plotted where the legend details the fraction of iron, silicates, and/or water for each color-coded curve.

are single stars (Winters et al. 2015, 2019a). Considering the occurrence rate of small planets with orbital period smaller than 10 days from Dressing & Charbonneau (2015) and combining with the transit probability of such planets (about a couple % to $\sim 20\%$), there would be a few to up to about twenty such planets.

The measured properties of L 168-9 b and its host star make it a promising target for the atmospheric characterization of a terrestrial planet via either transmission or emission spectroscopy measurements with JWST (Morley et al. 2017; Kempton et al. 2018) and/or thermal phase curve analysis to infer the absence of a thick atmosphere (e.g., Seager & Deming 2009). Its transmission and emission spectroscopy metrics from Kempton et al. (2018) are reported in Table 3 and compared to other confirmed transiting terrestrial planets with known masses that are of interest for atmospheric characterization. Based on this assessment, L 168-9 b is an excellent candidate for emission spectroscopy or for detecting the planetary day-side phase curve as recently done for the similar planet, LHS 3844 b (Kreidberg et al. 2019).

Acknowledgements. N. A.-D. acknowledges the support of FONDECYT project 3180063. J.K.T. acknowledges that support for this work was provided by NASA through Hubble Fellowship grant HST-HF2-51399.001 awarded by the Space Telescope Science Institute, which is operated by the Association of Universities for Research in Astronomy, Inc., for NASA, under contract NAS5-26555. R.B. acknowledges support from FONDECYT Post-doctoral Fellowship Project 3180246, and from the Millennium Institute of Astrophysics (MAS). X.B. and J.M.-A. acknowledge funding from the European Research Council under the ERC Grant Agreement n. 337591-ExTrA. X.D.; X.B.; T.F.; et L.M. acknowledge the support by the French National Research Agency in the framework of the Investissements d’Avenir program (ANR-15-IDEX-02), through the funding of the “Origin of Life” project of the Univ. Grenoble-Alpes.” LM acknowledge the support of the Labex OSUG@2020 (Investissements d’avenir – ANR10 LABX56). JRM acknowledges CAPES, CNPq and FAPERN Brazilian agencies. This work was supported by FCT/MCTES through national funds and by FEDER - Fundo Europeu de Desenvolvimento Regional through COMPETE2020 - Programa Operacional Competitividade e Internacionalização by these grants: UID/FIS/04434/2019; PTDC/FIS-AST/32113/2017 & POCI-01-0145-FEDER-032113; PTDC/FIS-AST/28953/2017 & POCI-01-0145-FEDER-028953. T.H. acknowledges support from the European Research Council under the Horizon 2020 Framework Program via the ERC Advanced Grant Origins 83 24 28. REM acknowledges support by the BASAL Centro de Astrofísica y Tecnologías Afines (CATA) and FONDECYT 1190621. A.J. acknowledges support from FONDECYT project 1171208 and by the Ministry for the Economy, De-

Table 2. Measured transit and RV model parameters of the L 168-9 planetary system.

Measured transit model parameters	TESS		
Baseline flux, γ_{TESS}	0.00001 ± 0.00029		
Orbital period, P_b [days]	1.40150 ± 0.00018		
Time of mid-transit, T_0 [BJD-2,457,000]	1340.04781 ^{+0.00088} _{-0.00122}		
Scaled semi-major axis, a/R_s	7.61 ± 0.31		
Planet-star radius ratio, r_p/R_s	0.0212 ± 0.001		
Orbital inclination, i [deg]	85.5 ^{+0.8} _{-0.7}		
Linear limb darkening coefficient, q_1	0.397 ^{+0.125} _{-0.111}		
Quadratic limb darkening coefficient, q_2	0.189 ^{+0.058} _{-0.056}		
TESS additive jitter, σ_{TESS}	0.00003 ^{+0.00011} _{-0.00003}		
Radial velocity GP hyperparameters	HARPS+PFS	HARPS	PFS
In HARPS covariance amplitude, $\ln(a_{\text{HARPS}}/\text{m s}^{-1})$	3.27 ^{+1.38} _{-1.03}	3.24 ^{+1.24} _{-1.19}	-
In PFS covariance amplitude, $\ln(a_{\text{PFS}}/\text{m s}^{-1})$	3.63 ^{+1.24} _{-1.08}	-	4.01 ^{+1.23} _{-0.97}
In RV exponential timescale, $\ln(\lambda_{\text{RV}}/\text{day})$	11.90 ^{+2.81} _{-1.99}	12.25 ^{+3.16} _{-2.18}	13.3 ^{+2.02} _{-1.44}
In RV coherence, $\ln(\Gamma_{\text{RV}})$	-0.09 ^{+0.20} _{-0.24}	-0.42 ^{+0.41} _{-0.55}	-0.22 ^{+0.39} _{-0.44}
In RV periodic timescale, $\ln(P_{\text{RV}}/\text{day})$	3.47 ^{+0.02} _{-0.03}	3.47 ^{+0.03} _{-0.03}	3.48 ^{+0.04} _{-0.03}
HARPS additive jitter, σ_{HARPS} [m s ⁻¹]	0.10 ^{+0.20} _{-0.09}	0.86 ^{+0.98} _{-0.86}	-
PFS additive jitter, σ_{PFS} [m s ⁻¹]	2.82 ± 0.42	-	2.78 ± 0.30
Measured RV model parameters	HARPS+PFS	HARPS	PFS
HARPS zero point velocity, γ_{HARPS} [km s ⁻¹]	29.7687 ± 0.0013	29.7692 ± 0.0013	-
PFS zero point velocity, γ_{PFS} [km s ⁻¹]	0.00077 ± 0.00186	-	0.00063 ± 0.00142
Semi-amplitude, K [m s ⁻¹]	3.66 ^{+0.47} _{-0.46}	3.74 ^{+0.54} _{-0.59}	3.26 ^{+0.52} _{-0.70}
$h = \sqrt{e} \cos \omega$	-0.10 ^{+0.17} _{-0.12}	0.04 ^{+0.15} _{-0.18}	-0.01 ^{+0.18} _{-0.21}
$k = \sqrt{e} \sin \omega$	0.00 ^{+0.17} _{-0.16}	-0.09 ^{+0.22} _{-0.23}	0.01 ^{+0.23} _{-0.30}
Derived L 168-9 b parameters	HARPS+PFS+TESS	HARPS+TESS	PFS+TESS
Semi-major axis, a [AU]	0.02091 ± 0.00024		
Equilibrium temperature, T_{eq} [K]			
Zero bond albedo	965 ± 20		
Venus-like bond albedo = 0.77	668 ± 14		
Planetary radius, R_p [R_{\oplus}]	1.39 ± 0.09		
Planetary mass, M_p [M_{\oplus}]	4.60 ± 0.56		
Planetary bulk density, ρ_p [g cm ⁻³]	9.6 ^{+2.4} _{-1.8}		
Planetary surface gravity, g_p [m s ⁻²]	23.9 ^{+4.5} _{-3.9}		
Planetary escape velocity, v_{esc} [km s ⁻¹]	20.5 ^{+1.4} _{-1.4}		
Orbital eccentricity, e^{\dagger}	< 0.21		
		4.74 ^{+0.71} _{-0.75}	4.08 ^{+0.70} _{-0.90}
		10.0 ^{+2.5} _{-1.9}	8.7 ^{+2.3} _{-2.1}
		24.4 ^{+4.8} _{-4.2}	21.4 ^{+4.4} _{-4.8}
		20.8 ^{+1.6} _{-1.7}	19.4 ^{+1.6} _{-2.2}
		< 0.25	< 0.26

[†] 95% confidence interval.

velopment, and Tourism's Programa Iniciativa Científica Milenio through grant IC 120009, awarded to the Millennium Institute of Astrophysics (MAS). JGW is supported by a grant from the John Templeton Foundation. The opinions expressed here are those of the authors and do not necessarily reflect the views of the John Templeton Foundation. Work J.N.W. was partly funded by the Heising-Simons Foundation. The authors would like to acknowledge Zachary Hartman for his help conducting the Gemini-South/DSSI observations. Some of the work here is based on observations obtained at the Gemini Observatory, which is operated by the Association of Universities for Research in Astronomy, Inc., under a cooperative agreement with the NSF on behalf of the Gemini partnership: the National Science Foundation (United States), National Research Council (Canada),

CONICYT (Chile), Ministerio de Ciencia, Tecnología e Innovación Productiva (Argentina), Ministério da Ciência, Tecnologia e Inovação (Brazil), and Korea Astronomy and Space Science Institute (Republic of Korea). This work makes use of observations from the LCOGT network. Funding for the TESS mission is provided by NASA's Science Mission directorate. We acknowledge the use of public TESS Alert data from pipelines at the TESS Science Office and at the TESS Science Processing Operations Center. This research has made use of the Exoplanet Follow-up Observation Program website, which is operated by the California Institute of Technology, under contract with the National Aeronautics and Space Administration under the Exoplanet Exploration Program. Resources supporting this work were provided by the NASA High-End Computing (HEC)

Table 3. Prospects of atmospheric characterization of confirmed terrestrial planets including L 168-9 b. TSM and ESM correspond to transmission and emission spectroscopy metrics, respectively.

Star ID	R_p	M_p	P	a	T_{eff}	T_{eq}	T_{day}	J	K_s	R_*	M_*	TSM	ESM	Ref.
units	[R_\oplus]	[M_\oplus]	[days]	[AU]	[K]	[K]	[K]	[mag]	[mag]	[R_\odot]	[M_\odot]			
L 168-9 b	1.39	4.39	1.401	0.021	3743	963.01	1059.31	7.941	7.0819	0.60	0.62	8.025	9.692	
LHS 3844 b	1.30	–	0.463	0.006	3036	805.90	886.49	10.046	9.145	0.19	0.15	–	29.004	Kr2019
GJ 1132 b	1.13	1.66	1.629	0.015	3270	590.61	649.67	9.245	8.322	0.21	0.18	31.166	9.872	Bo2018
L 98-59 c	1.35	2.17	3.690	0.032	3412	515.31	566.84	7.933	7.101	0.31	0.31	29.168	6.696	Cl2019b
LTT 1445A b	1.38	2.20	5.359	0.038	3335	433.34	476.68	7.29	6.5	0.28	0.26	44.976	6.382	Wi2019
TRAPPIST-1 b	1.09	1.02	1.511	0.011	2559	402.38	442.62	11.4	10.3	0.12	0.08	36.914	4.007	Gi2017
LHS 1140 c	1.28	1.81	3.778	0.027	3216	436.43	480.07	9.612	8.821	0.21	0.18	25.225	3.401	Me2019

Reference notes: Kr2019 – (Kreidberg et al. 2019); Bo2018 – Bonfils et al. (2018); Cl2019b – Cloutier, R. et al. (2019); Wi2019 – Winters et al. (2019b); Gi2017 – Gillon et al. (2017); Me2019 – Ment et al. (2019);

Program through the NASA Advanced Supercomputing (NAS) Division at Ames Research Center for the production of the SPOC data products. This paper includes data collected by the TESS mission, which are publicly available from the Mikulski Archive for Space Telescopes (MAST). This research has made use of the NASA Exoplanet Archive, which is operated by the California Institute of Technology, under contract with the National Aeronautics and Space Administration under the Exoplanet Exploration Program.

References

- Allard, F. 2014, in IAU Symposium, Vol. 299, Exploring the Formation and Evolution of Planetary Systems, ed. M. Booth, B. C. Matthews, & J. R. Graham, 271–272
- Anglada-Escudé, G. & Butler, R. P. 2012, The Astrophysical Journal Supplement Series, 200, 15
- Angus, R., Morton, T., Aigrain, S., Foreman-Mackey, D., & Rajpaul, V. 2018, MNRAS, 474, 2094
- Astudillo-Defru, N., Delfosse, X., Bonfils, X., et al. 2017a, A&A, 600, A13
- Astudillo-Defru, N., Díaz, R. F., Bonfils, X., et al. 2017b, A&A, 605, L11
- Astudillo-Defru, N., Forveille, T., Bonfils, X., et al. 2017c, A&A, 602, A88
- Baranne, A., Queloz, D., Mayor, M., et al. 1996, A&AS, 119, 373
- Barragán, O., Gandolfi, D., Dai, F., et al. 2018, A&A, 612, A95
- Batalha, N. E., Lewis, T., Fortney, J. J., et al. 2019, ApJ, 885, L25
- Bayo, A., Rodrigo, C., Barrado Y Navascués, D., et al. 2008, A&A, 492, 277
- Beichman, C. A., Bryden, G., Stapelfeldt, K. R., et al. 2006, ApJ, 652, 1674
- Bonfils, X., Almenara, J.-M., Cloutier, R., et al. 2018, A&A, 618, A142
- Brown, T. M., Baliber, N., Bianco, F. B., et al. 2013, PASP, 125, 1031
- Butler, R. P., Marcy, G. W., Williams, E., et al. 1996, PASP, 108, 500
- Charbonneau, D., Brown, T. M., Latham, D. W., & Mayor, M. 2000, ApJ, 529, L45
- Ciardi, D. R., Beichman, C. A., Horch, E. P., & Howell, S. B. 2015, ApJ, 805, 16
- Cloutier, R., Astudillo-Defru, N., Doyon, R., et al. 2017, A&A, 608, A35
- Cloutier, R., Astudillo-Defru, N., Doyon, R., et al. 2019, A&A, 621, A49
- Cloutier, R. & Menou, K. 2019, arXiv e-prints, arXiv:1912.02170
- Cloutier, R., Astudillo-Defru, N., Bonfils, X., et al. 2019, A&A, 629, A111
- Collins, K. A., Kielkopf, J. F., Stassun, K. G., & Hessman, F. V. 2017, AJ, 153, 77
- Crane, J. D., Shectman, S. A., & Butler, R. P. 2006, in Proc. SPIE, Vol. 6269, Society of Photo-Optical Instrumentation Engineers (SPIE) Conference Series, 626931
- Crane, J. D., Shectman, S. A., Butler, R. P., et al. 2010, in Proc. SPIE, Vol. 7735, Ground-based and Airborne Instrumentation for Astronomy III, 773553
- Crane, J. D., Shectman, S. A., Butler, R. P., Thompson, I. B., & Burley, G. S. 2008, in Proc. SPIE, Vol. 7014, Ground-based and Airborne Instrumentation for Astronomy II, 701479
- Cutri, R. M. & et al. 2013, VizieR Online Data Catalog, II/328
- Cutri, R. M., Skrutskie, M. F., van Dyk, S., et al. 2003, VizieR Online Data Catalog, II/246
- de Zeeuw, T., Tamai, R., & Liske, J. 2014, The Messenger, 158, 3
- Dressing, C. D. & Charbonneau, D. 2015, ApJ, 807, 45
- Dumusque, X., Turner, O., Dorn, C., et al. 2019, A&A, 627, A43
- Espinoza, N., Brahm, R., Henning, T., et al. 2019, arXiv e-prints, arXiv:1903.07694
- Faria, J. P., Haywood, R. D., Brewer, B. J., et al. 2016, A&A, 588, A31
- Foreman-Mackey, D., Hogg, D. W., Lang, D., & Goodman, J. 2013, PASP, 125, 306
- Fulton, B. J., Petigura, E. A., Howard, A. W., et al. 2017, AJ, 154, 109
- Gaia Collaboration. 2018, VizieR Online Data Catalog, I/345
- Gaidos, E., Mann, A. W., Lépine, S., et al. 2014, MNRAS, 443, 2561
- Gandolfi, D., Barragán, O., Hatzes, A. P., et al. 2017, AJ, 154, 123
- Gardner, J. P., Mather, J. C., Clampin, M., et al. 2006, Space Sci. Rev., 123, 485
- Giles, H. A. C., Collier Cameron, A., & Haywood, R. D. 2017, MNRAS, 472, 1618
- Gillon, M., Triard, A. H. M. J., Demory, B.-O., et al. 2017, Nature, 542, 456
- Goodman, J. & Weare, J. 2010, Communications in Applied Mathematics and Computational Science, Vol. 5, No. 1, p. 65-80, 2010, 5, 65
- Grunblatt, S. K., Howard, A. W., & Haywood, R. D. 2015, ApJ, 808, 127
- Guenther, E. W., Barragán, O., Dai, F., et al. 2017, A&A, 608, A93
- Hauschildt, P. H., Allard, F., & Baron, E. 1999, ApJ, 512, 377
- Haywood, R. D., Collier Cameron, A., Queloz, D., et al. 2014, MNRAS, 443, 2517
- Henden, A. A., Templeton, M., Terrell, D., et al. 2016, VizieR Online Data Catalog, II/336
- Henry, G. W., Marcy, G. W., Butler, R. P., & Vogt, S. S. 2000, ApJ, 529, L41
- Hög, E., Fabricius, C., Makarov, V. V., et al. 2000, A&A, 355, L27
- Horch, E. P., Gomez, S. C., Sherry, W. H., et al. 2011, AJ, 141, 45
- Horch, E. P., Howell, S. B., Everett, M. E., & Ciardi, D. R. 2012, AJ, 144, 165
- Horch, E. P., Veillette, D. R., Baena Gallé, R., et al. 2009, AJ, 137, 5057
- Howell, S. B., Everett, M. E., Sherry, W., Horch, E., & Ciardi, D. R. 2011, AJ, 142, 19
- Jenkins, J. M., Twicken, J. D., McCauliff, S., et al. 2016, in Society of Photo-Optical Instrumentation Engineers (SPIE) Conference Series, Vol. 9913, Software and Cyberinfrastructure for Astronomy IV, 99133E
- Jensen, E. 2013, Tapir: A web interface for transit/eclipse observability, Astrophysics Source Code Library
- Kempton, E. M.-R., Bean, J. L., Louie, D. R., et al. 2018, PASP, 130, 114401
- Kipping, D. M. 2013, MNRAS, 435, 2152
- Kreidberg, L., Koll, D. D. B., Morley, C., et al. 2019, arXiv e-prints, arXiv:1908.06834
- Lam, K. W. F., Santerne, A., Sousa, S. G., et al. 2018, A&A, 620, A77
- Lo Curto, G., Pepe, F., Avila, G., et al. 2015, The Messenger, 162, 9
- López-Morales, M., Haywood, R. D., Coughlin, J. L., et al. 2016, AJ, 152, 204
- Lovis, C. & Pepe, F. 2007, A&A, 468, 1115
- Luque, R., Pallé, E., Kossakowski, D., et al. 2019, A&A, 628, A39
- Mandel, K. & Agol, E. 2002, ApJ, 580, L171
- Mann, A. W., Dupuy, T., Kraus, A. L., et al. 2019, ApJ, 871, 63
- Mayor, M., Pepe, F., Queloz, D., et al. 2003, The Messenger, 114, 20
- Mazeh, T., Naef, D., Torres, G., et al. 2000, ApJ, 532, L55
- Ment, K., Dittmann, J. A., Astudillo-Defru, N., et al. 2019, AJ, 157, 32
- Moór, A., Ábrahám, P., Derekas, A., et al. 2006, ApJ, 644, 525
- Morley, C. V., Kreidberg, L., Rustamkulov, Z., Robinson, T., & Fortney, J. J. 2017, ApJ, 850, 121
- Mortier, A., Faria, J. P., Santos, N. C., et al. 2016, A&A, 585, A135
- Motalebi, F., Udry, S., Gillon, M., et al. 2015, A&A, 584, A72
- Muirhead, P. S., Dressing, C. D., Mann, A. W., et al. 2018, AJ, 155, 180
- Neves, V., Bonfils, X., Santos, N. C., et al. 2014, A&A, 568, A121
- Pollacco, D. L., Skillen, I., Collier Cameron, A., et al. 2006, PASP, 118, 1407
- Queloz, D., Henry, G. W., Sivan, J. P., et al. 2001, A&A, 379, 279
- Rice, K., Malavolta, L., Mayo, A., et al. 2019, Monthly Notices of the Royal Astronomical Society, 484, 3731
- Ricker, G. R., Winn, J. N., Vanderspek, R., et al. 2015, Journal of Astronomical Telescopes, Instruments, and Systems, 1, 014003
- Santerne, A., Brugger, B., Armstrong, D. J., et al. 2018, Nature Astronomy, 2, 393

- Seager, S. & Deming, D. 2009, *ApJ*, 703, 1884
- Smith, J. C., Stumpe, M. C., Van Cleve, J. E., et al. 2012, *PASP*, 124, 1000
- Stassun, K. G., Collins, K. A., & Gaudi, B. S. 2017, *AJ*, 153, 136
- Stassun, K. G., Corsaro, E., Pepper, J. A., & Gaudi, B. S. 2018a, *AJ*, 155, 22
- Stassun, K. G., Oelkers, R. J., Pepper, J., et al. 2018b, *AJ*, 156, 102
- Stassun, K. G. & Torres, G. 2016, *AJ*, 152, 180
- Stassun, K. G. & Torres, G. 2018, *ApJ*, 862, 61
- Stumpe, M. C., Smith, J. C., Catanzarite, J. H., et al. 2014, *PASP*, 126, 100
- Sullivan, P. W., Winn, J. N., Berta-Thompson, Z. K., et al. 2015, *ApJ*, 809, 77
- Teske, J. K., Ciardi, D. R., Howell, S. B., Hirsch, L. A., & Johnson, R. A. 2018, *AJ*, 156, 292
- Teske, J. K., Shectman, S. A., Vogt, S. S., et al. 2016, *AJ*, 152, 167
- Tokovinin, A. 2018, *PASP*, 130, 035002
- Twicken, J. D., Catanzarite, J. H., Clarke, B. D., et al. 2018, *Publications of the Astronomical Society of the Pacific*, 130, 064502
- Wang, S., Wu, D.-H., Barclay, T., & Laughlin, G. P. 2017, *arXiv e-prints*, arXiv:1704.04290
- Winters, J. G., Henry, T. J., Jao, W.-C., et al. 2019a, *AJ*, 157, 216
- Winters, J. G., Henry, T. J., Lurie, J. C., et al. 2015, *AJ*, 149, 5
- Winters, J. G., Medina, A. A., Irwin, J. M., et al. 2019b, *AJ*, 158, 152
- Zechmeister, M. & Kürster, M. 2009, *A&A*, 496, 577
- Ziegler, C., Law, N. M., Baranec, C., et al. 2018, *AJ*, 155, 161
- Ziegler, C., Tokovinin, A., Briceno, C., et al. 2019, *arXiv e-prints*, arXiv:1908.10871
- cepción, Chile
E-mail: nastudillo@ucsc.cl
- ² Center for Astrophysics | Harvard & Smithsonian, 60 Garden Street, Cambridge, MA 02138, USA
- ³ Dept. of Astronomy & Astrophysics, University of Toronto, 50 St. George Street, Toronto, ON, M5S 3H4, Canada
- ⁴ Observatories of the Carnegie Institution for Science, 813 Santa Barbara Street, Pasadena, CA 91101
- ⁵ NASA Hubble Fellow
- ⁶ Center of Astro-Engineering UC, Pontificia Universidad Católica de Chile, Av. Vicuña Mackenna 4860, 7820436 Macul, Santiago, Chile
- ⁷ Instituto de Astrofísica, Facultad de Física, Pontificia Universidad Católica de Chile, Av. Vicuña Mackenna 4860, 7820436 Macul, Santiago, Chile
- ⁸ Millennium Institute of Astrophysics, Chile
- ⁹ Astrophysics Group, Keele University, Staffordshire, ST5 5BG, UK
- ¹⁰ Kavli Institute for Astrophysics and Space Research, Massachusetts Institute of Technology, Cambridge, MA 02139, USA
- ¹¹ Department of Earth, Atmospheric, and Planetary Sciences, Massachusetts Institute of Technology, Cambridge, MA 02139, USA
- ¹² Department of Astrophysical Sciences, Princeton University, Princeton, NJ 08544, USA
- ¹³ NASA Ames Research Center, Moffett Field, CA 94035, USA
- ¹⁴ Department of Physics and Astronomy, Vanderbilt University, Nashville, TN 37235, USA
- ¹⁵ Dunlap Institute for Astronomy and Astrophysics, University of Toronto, Ontario M5S 3H4, Canada
- ¹⁶ Univ. Grenoble Alpes, CNRS, IPAG, F-38000 Grenoble, France
- ¹⁷ Department of Physics, University of Warwick, Gibbet Hill Road, Coventry CV4 7AL, UK
- ¹⁸ Institut de Recherche sur les Exoplanètes, Département de Physique, Université de Montréal, Montréal QC, H3C 3J7, Canada
- ¹⁹ Observatoire de Genève, Université de Genève, 51 ch. des Maillettes, 1290 Sauverny, Switzerland
- ²⁰ Cerro Tololo Inter-American Observatory, Casilla 603, La Serena, Chile
- ²¹ Department of Terrestrial Magnetism, Carnegie Institution for Science, 5241 Broad Branch Road NW, Washington DC 20015, USA
- ²² American Association of Variable Star Observers, 49 Bay State Road, Cambridge, MA 02138, USA
- ²³ Department of Physics, and Kavli Institute for Astrophysics and Space Research, Massachusetts Institute of Technology, Cambridge, MA, USA
- ²⁴ Physics & Astronomy Department, University of Kansas, Lawrence, KS, 66044, USA
- ²⁵ Universidad de Buenos Aires, Facultad de Ciencias Exactas y Naturales, Buenos Aires, Argentina
- ²⁶ CONICET - Universidad de Buenos Aires. Instituto de Astronomía y Física del Espacio (IAFE), Buenos Aires, Argentina
- ²⁷ Department of Physics and Astronomy, University of New Mexico, Albuquerque, NM, USA
- ²⁸ Space Telescope Science Institute, 3700 San Martin Drive, Baltimore, MD 21218
- ²⁹ European Southern Observatory, Alonso de Córdova 3107, Vitacura, Región Metropolitana, Chile
- ³⁰ Universidad de Concepción, Departamento de Astronomía, Casilla 160-C, Concepción, Chile
- ³¹ Physics Department and Tsinghua Centre for Astrophysics, Tsinghua University, Beijing 100084, China
- ³² Centre for Astrophysics, University of Southern Queensland, Toowoomba, QLD, 4350, Australia
- ³³ Max-Planck-Institut für Astronomie, Königstuhl 17, D-69117 Heidelberg, Germany
- ³⁴ Department of Physics, Southern Connecticut State University, 501 Crescent Street, New Haven, CT 06515, USA
- ³⁵ Campo Catino Astronomical Observatory, Regione Lazio, Guarcino (FR), 03010 Italy
- ³⁶ Departamento de Astronomía, Universidad de Chile, Camino El Observatorio 1515, Las Condes, Santiago, Chile
- ³⁷ Facultad de Ingeniería y Ciencias, Universidad Adolfo Ibáñez, Av. Diagonal las Torres 2640, Peñalolén, Santiago, Chile
- ³⁸ Department of Physics and Astronomy, University of Louisville, Louisville, KY 40292, USA
- ³⁹ Department of Physics and Astronomy, The University of North Carolina at Chapel Hill, Chapel Hill, NC 27599-3255, USA
- ⁴⁰ Departamento de Física Universidade Federal do Rio Grande do

¹ Departamento de Matemática y Física Aplicadas, Universidad Católica de la Santísima Concepción, Alonso de Rivera 2850, Con-

Appendix A: Gaussian process model

Gaussian process (GP) regression is widely used in the exoplanet community as a non-parametric Bayesian approach to model temporally correlated stellar activity signals in RV data. These rotationally-modulated activity signals prohibit the accurate measurement of planetary parameters and often produce in planetary false positives.

Here we model the RV activity signals of L 168-9 as a stochastic process whose temporal evolution is well-described by a quasi-periodic covariance kernel. A GP with a quasi-periodic covariance kernel $k(t_i, t_j)$ is included in our joint model describing the data RV and transit data and takes the following form:

$$k(t_i, t_j) = a^2 \exp \left[-\frac{(t_i - t_j)^2}{2\lambda^2} - \Gamma^2 \sin^2 \left(\frac{\pi |t_i - t_j|}{P_{\text{GP}}} \right) \right] \quad (\text{A.1})$$

and is described by the covariance amplitude a , the exponential evolutionary timescale λ , the coherence Γ , and the periodic timescale P_{GP} .

As usual in the Bayesian context, prior probability density functions (PDF) for the hyperparameters $\{a, \lambda, \Gamma, P_{\text{GP}}\}$ are listed in Table A.1 for the multiple GPs applied our data analysis. The posterior PDF are sampled through a Markov chain Monte Carlo (MCMC, [Goodman & Weare 2010](#)); in particular we used the emcee ensemble sampler ([Foreman-Mackey et al. 2013](#)). The sampling of the joint posterior is made with the Gaussian ln likelihood function given by

$$\ln \mathcal{L} = -\frac{1}{2} (y^{\text{T}} \cdot K \cdot y + \ln \det K + N \ln 2\pi) \quad (\text{A.2})$$

where y is the vector of N measurement taken at times $t = \{t_1, t_2, \dots, t_N\}$ and the $N \times N$ covariance matrix K is given by

$$K_{ij} = k(t_i, t_j) + \delta_{ij} [\sigma(t_i)^2 + s^2]. \quad (\text{A.3})$$

being δ_{ij} the Kronecker delta that adds the measurement uncertainties σ to the diagonal elements of K and includes an additive jitter factor s .

Appendix B: Spectroscopic Data

Table A.1. L 168-9 model parameter priors.

Parameter	Prior
Photometry model	
Baseline flux, γ_{TESS}	$\mathcal{U}(-0.1, 0.1)$
Limb darkening coefficient, u_1	$\mathcal{U}(0.1, 0.4)$
Limb darkening coefficient, u_2	$\mathcal{U}(0.25, 0.55)$
TESS additive jitter, s_{TESS}	$\mathcal{J}(10^{-2}, 1)$
RV model	
HARPS zero point velocity, $\gamma_{0,\text{HARPS}}$ [m s ⁻¹]	$\mathcal{U}(-1, 1)$
PFS zero point velocity, $\gamma_{0,\text{PFS}}$ [m s ⁻¹]	$\mathcal{U}(-1, 1)$
ln HARPS covariance amplitude, ln ($a_{\text{HARPS}}/\text{m s}^{-1}$)	$\mathcal{U}(-5, 10)$
ln PFS covariance amplitude, ln ($a_{\text{PFS}}/\text{m s}^{-1}$)	$\mathcal{U}(-5, 10)$
ln RV exponential time scale, ln ($\lambda_{\text{RV}}/\text{day}$)	From H α training
ln RV coherence, ln (Γ_{RV})	From H α training
ln RV periodic timescale, ln (P_{RV}/day)	From H α training
HARPS additive jitter, s_{HARPS} [m s ⁻¹]	$\mathcal{J}(10^{-2}, 10)$
PFS additive jitter, s_{PFS} [m s ⁻¹]	$\mathcal{J}(10^{-2}, 10)$
<i>L 168-9 b (TOI-134.01)</i>	
Orbital period, P_b [days]	$\mathcal{U}(1.370, 1.405)$
Time of mid-transit, $T_{0,b}$ [BJD - 2,457,000]	$\mathcal{U}(1338, 1342)$
Scaled semi-major axis, a/R_s	$\mathcal{G}(7.542, 0.27)$
Planet-star radius ratio, r_p/R_s	$\mathcal{U}(0, 0.1)$
Orbital inclination, i [deg]	$\mathcal{U}(75, 105)$
Semi-amplitude, K_b [m s ⁻¹]	$\mathcal{J}(10^{-2}, 10)$
$h_b = \sqrt{e_b} \cos \omega_b$	$\mathcal{U}(-1, 1)$
$k_b = \sqrt{e_b} \sin \omega_b$	$\mathcal{U}(-1, 1)$

Table B.1. HARPS radial velocity time series and spectroscopic activity indicators for L 168-9 (minimal, full version available at the CDS).

BJD [-2450000]	RV [$m s^{-1}$]	σ_{RV} [$m s^{-1}$]	H α	$\sigma_{H\alpha}$	H β	$\sigma_{H\beta}$	H γ	$\sigma_{H\gamma}$	NaD	σ_{NaD}	S	σ_S
4664.954608	29781.65	3.48	0.06224	0.00025	0.04679	0.00052	0.10087	0.00131	0.01232	0.00020	1.616	0.068
4991.927461	29786.04	2.95	0.06074	0.00021	0.04632	0.00044	0.10385	0.00114	0.01172	0.00016	2.167	0.073
8367.523380	29769.97	1.37	0.05962	0.00011	0.04606	0.00019	0.10582	0.00052	0.01166	0.00007	1.892	0.018
8367.551447	29773.09	1.19	0.05928	0.00010	0.04534	0.00016	0.10573	0.00045	0.01158	0.00006	1.826	0.014
8367.623921	29772.57	1.20	0.05944	0.00010	0.04562	0.00017	0.10639	0.00046	0.01164	0.00006	1.868	0.014

Table B.2. PFS radial velocity time series and spectroscopic activity indicators (minimal, full version available at the CDS).

BJD [-2450000]	RV [$m s^{-1}$]	σ_{RV} [$m s^{-1}$]	H α	S
8409.51799	8.80	1.74	1.293	0.05807
8409.53206	4.10	1.74	1.334	0.05813
8409.60491	-3.11	1.71	1.285	0.05879
8409.61960	4.80	1.75	1.340	0.05901
8409.67495	8.23	2.09	1.311	0.05976